Band alignments through quasiparticle self-consistent *GW* with efficient vertex corrections

Arnaud Lorin, Thomas Bischoff, Alexey Tal, and Alfredo Pasquarello
Chaire de Simulation à l'Echelle Atomique (CSEA), Ecole Polytechnique Fédérale de Lausanne (EPFL), 1015 Lausanne, Switzerland

(Received 24 March 2023; accepted 25 October 2023; published 5 December 2023)

Within many-body perturbation theory, we calculate band offsets for a set of epitaxial interfaces, including AlP/GaP, AlAs/GaAs, Ge/AlAs, Ge/GaAs, Ge/ZnSe, Si/GaP, ZnSe/GaAs, and CaF_2/Si. We consider various quasiparticle self-consistent *GW* schemes with or without including vertex functions. In particular, we consider two types of effective vertex functions complying with the Ward identity in the long range, one of which additionally carries a short-range part, which has been found to improve ionization potentials. The obtained band offsets correspond to model interface structures that match the experimental lattice parameters of the bulk components. Strain, zero-phonon renormalization, and spin-orbit coupling effects are properly accounted for. For the band offsets of the semiconductor-semiconductor interfaces, all the self-consistent *GW* schemes yield similar mean absolute errors on the order of 0.2 eV. In the case of the CaF_2/Si interface, the calculated band offsets show large indetermination spanning an interval up to 1 eV, the discrepancy with respect to experiment being correlated with the error by which the band gap of the insulator is described. Through *GW* calculations for selected interface models, we further assess the effect of self-consistently updating the charge density. Our result support the practice of relying on semilocal or hybrid-functional schemes for determining the line-up potential.

DOI: 10.1103/PhysRevB.108.245303

I. INTRODUCTION

Semiconductor-semiconductor and insulator-semiconductor heterostructures are found in essentially all modern electronic, photovoltaic, and photocatalytic devices [1–6]. The interest in heterostructures stems from the occurrence of valence and conduction band offsets, which affect the dynamics of electrons and holes across interfaces. The usefulness of accurate theoretical schemes also underlies the determination of Schottky barrier heights at metal-semiconductor interfaces in nanoelectronics, insofar no Fermi-level pinning occurs due to uncharacterized interface defects [7,8]. To design optimal devices, it is therefore important to develop theoretical methods that are able to provide accurate predictions of band offsets.

Numerous electronic-structure calculations can be found in the literature [9–19]. Most of these studies are based on density functional theory (DFT) [20,21], either at the semilocal or at hybrid functional level. In order to properly predict band offsets, it is a prerequisite for the adopted electronic structure method to achieve accurate band gaps [13,14]. This holds both for conduction and valence band offsets despite the common belief that ground-state DFT should be accurate for valence band levels. Semilocal DFT is generally unsatisfactory due to the well-known band-gap problem [22,23]. To overcome this problem, one possibility is to turn to hybrid functionals [24–26], which noticeably open up the band gap. Indeed, an improvement in the calculated band offsets is found with standard hybrid functionals, such as PBE0 and HSE [13,27]. However, to improve the accuracy further, it is generally necessary to set the mixing parameters in an empirical fashion in order to retrieve the correct band gaps of the interface components [13,15,27]. In this context, the variation of the optimal mixing parameter across the interface introduces a supplementary problem associated with the use of spatial-dependent hybrid functionals [28,29].

The state-of-the-art scheme for electronic-structure calculations presently relies on many-body perturbation theory, which is based on a Green's function formulation [30]. A multitude of flavors have appeared in the literature. The simplest one is the one-shot G_0W_0 approximation [31], in which no self-consistent cycle is carried out, thereby leading to an undesired dependence on the starting wave functions and energy levels [32]. The quasiparticle selfconsistent *GW* scheme, denoted qs*GW*, suppresses the dependence on starting point [33,34], but this method typically yields band-gap overestimations of about 20% [32,33,35–37], which can be related to the neglect of the vertex function [32,33,35–37]. Inclusion of approximated vertex corrections [37–39] in the polarizability has been shown to reduce this overestimation [35–37,40,41]. The nanoquanta vertex function was found to be very accurate for band-gap evaluations, but requires the computationally demanding solution of the Bethe-Salpeter equation [35,38,40]. The empirical Bootstrap kernel [39] avoids the Bethe-Salpeter equation and has been found to reproduce band gaps with essentially the same accuracy as the nanoquanta vertex [36]. More recently, an effective vertex kernel could be constructed in a nonempirical fashion by satisfying the Ward identity in the long range, leading to the description of band gaps with a mean absolute error of about 0.2 eV on an extended set of materials [37].

The proper description of bulk band gaps is not a sufficient condition to achieve accurate band offsets. It is also necessary to obtain a reliable relative alignment of the electronic

structures of the interface components. To achieve such an alignment, several issues have to be addressed. The main issue concerns the intrinsic accuracy of the adopted electronic-structure theory. In this regard, the absolute alignment of the band-edge energy with respect to the vacuum level has often been taken as a convenient benchmark [32,36,37,41–43]. It has been found that hybrid functionals generally give a very good description of electron affinities and ionization potentials when they accurately describe the band gap [32,42,43]. In many-body perturbation theory, achieving the correct alignment appears more challenging [32,36,37,41,42]. Grüneis *et al.* have shown that the achievement of accurate ionization potentials requires the treatment of the vertex function up to second order [41] for improving upon ordinary *GW* schemes [32,37,42]. It has been found that such an accuracy cannot be achieved through the inclusion of effective vertex functions in the sole polarizability [36,37]. However, noticeably improved ionization potentials are obtained when a short-range vertex is included in the self-energy [37,44]. When the effective vertex includes both short-range and long-range parts like in qs$G\hat{W}$, the mean accuracy of ionization potentials amounts to 0.3 eV [37].

Several additional challenges need to be overcome to achieve accurate band offsets at interfaces. The actual interface structure used in the calculations is generally unknown and needs to be modeled. Residual strain effects resulting from structural mismatch to the substrate may also play a role [16,18]. Furthermore, high-level *GW* calculations with vertex corrections require a self-consistent treatment of the charge density. The state-of-the-art approach to calculate band offsets at interfaces relies on separate calculations of the bulk interface components combined with an interface calculation for determining the line-up of the reference potential [9,11]. One of the advantages of this scheme is that the reference potential converges at small distance from the interface, thereby allowing for the use of interface models of affordable size. In addition, a further computational advantage is that the line-up potential is generally determined at the semilocal density-functional level [14–16,18,41,42,45]. Thus, the self-consistency at interfaces has rarely been investigated at the *GW* level of theory [14]. The justification for using a semilocal scheme for determining the potential line-up rests on the study of the Si/SiO_2 interface, which remains so far the sole case where this approximation has been validated through self-consistent updates of the charge density [14]. Further support to this practice also comes from hybrid-functional calculations, which show that the band line-up only weakly depends on the adopted fraction of Fock exchange [13,15,18]. Hence, the combination of such structural and electronic issues makes of the calculation of band alignments at interfaces a noticeable theoretical challenge.

In this paper, we determine band offsets for various epitaxial interfaces through quasiparticle self-consistent *GW* calculations including vertex corrections. We adopt an approach based on the line-up of bulk calculations through the electrostatic potential determined at the interface. The investigated set includes semiconductor-semiconductor interfaces involving group III, IV, and V materials, viz., AlP/GaP, AlAs/GaAs, Ge/AlAs, Ge/GaAs, Ge/ZnSe, Si/GaP, ZnSe/GaAs, as well one insulator-semiconductor interface, namely CaF_2/Si. The study of the latter interface between wide and narrow band-gap materials is expected to be less subject to error-cancellation effects resulting from the similar nature of the bulk components, as is the case for the semiconductor-semiconductor interfaces [15,18]. In particular, two types of effective vertex functions complying with the Ward identity in the long range [37] are used in this investigation. The first one gives rise to qs$G\tilde{W}^{\mathrm{LR}}$ calculations, where the long-range vertex function occurs in the polarizability and is effectively canceled in the self-energy [34,37]. In qs$G\hat{W}$ calculations, the vertex function intervenes in both the polarizability and the self-energy. This vertex additionally carries a short-range part derived from the adiabatic local density approximation (ALDA) [46], which is expected to improve the accuracy of ionization potentials [37,44]. The use of epitaxial interfaces facilitates the construction of accurate model structures. The determined band offsets are obtained for interface structures matching experimental lattice parameters for the bulk components. In this regard, attention is devoted to distinguishing the substrate and overlayer components, whereby the strain effects on the latter are taken into account [18]. Finally, for two interfaces (AlP/GaP and CaF_2/Si), we investigate at the qs$G\hat{W}$ level to what extent the line-up potential is affected by the self-consistent update of the charge density, in comparison with semilocal and hybrid-functional results.

This article is organized as follows. In Sec. II, the *GW* schemes and the methodology for obtaining band offsets are described. The bands gaps and the alignment of the electronic structure with respect to the average electrostatic potential for the involved materials are the topic of Sec. III. In Sec. IV, the line-up potentials are determined and the band offsets calculated. The conclusions are drawn in Sec. V.

II. METHODOLOGY

A. *GW* schemes with effective vertices

Many-body perturbation theory is the state of the art for describing the electronic structure of extended systems. This theory relies on a set of equations involving the Green's function G, as first proposed by Hedin [30]. Within Hedin's equations, the self-energy is written as

$$\Sigma = iGW\Gamma, \tag{1}$$

where W is the screened Coulomb potential. The vertex Γ occurs in the calculation of both the self-energy Σ and the screened potential W. When an effective vertex function is included in the screening, the band gaps are found to improve significantly [35–37,40,41]. It has also been shown that the consideration of a vertex function in the self-energy primarily leads to an overall shift of the energy levels, while leaving the band gap relatively unchanged [14,47,48].

Recently, two effective vertex functions satisfying the Ward identity in the long range have been introduced and shown to give accurate band gaps and ionization potentials for a large set of materials [49]. The Ward identity is an exact constraint enforcing the conservation of the total charge [50,51]. The vertex is then approximated as [52]

$$\Gamma = 1 + f_{\mathrm{xc}}\chi, \tag{2}$$

where f_{xc} is an effective exchange-correlation kernel and χ is the irreducible polarizability. The exchange and correlation kernel is split into a long-range and a short-range part, $f_{xc} = f^{LR} + f^{SR}$ [49]. Using the Ward identity, the long-range part of the kernel can be written as

$$f^{LR} = \frac{1 - Z}{\chi^0_{00}}, \tag{3}$$

where Z is the renormalization factor defined by $Z = (1 - \frac{\partial \Sigma}{\partial \omega})^{-1}$ and χ^0 is the independent particle polarizability. The self-energy can then be rewritten as

$$\Sigma = iG^0\hat{W}, \tag{4}$$

where G^0 is the coherent part of the Green's function, which is reduced by a factor Z, $G \approx ZG^0$, and where the modified screened potential is written as

$$\hat{W} = v + (v + Zf^{SR})\chi^{red}v. \tag{5}$$

Here, χ^{red} is the reducible polarizability and f^{SR} is the short-range part of the exchange-correlation kernel, which is chosen to be the adiabatic local density approximation (ALDA) [46]. This scheme is denoted qs$G\hat{W}$. The qs$G\tilde{W}^{LR}$ approximation is similar to the qs$G\hat{W}$ one, but only includes the long-range part of the exchange-correlation kernel (i.e., $f^{SR} = 0$). The self-energy then reads

$$\Sigma = iG^0\tilde{W}, \tag{6}$$

with $\tilde{W} = v + v\chi^{red}v$. In all cases, the reducible polarizability χ^{red} is determined from

$$\chi^{red} = \chi^0 + \chi^0(v + f_{xc})\chi^{red}, \tag{7}$$

where the kernel $f_{xc} = f^{LR} + f^{SR}$ and $f_{xc} = f^{LR}$ in the qs$G\hat{W}$ and qs$G\tilde{W}^{LR}$ schemes, respectively. In this way, the vertex corrections are included in both the screening and the self-energy. For completeness, we include in the present study results achieved with the state-of-the-art NANOQUANTA kernel, which we denote qs$G\tilde{W}^{NQ}$ [35,38,40]. We also add qs$G\tilde{W}^{Boot}$ results achieved with the Bootstrap kernel [39], which has been shown to give band gaps closely reproducing those obtained with qs$G\tilde{W}^{NQ}$ for a variety of materials [36].

In this paper, we carry out all the *GW* calculations with the VASP suite [53,54], in particular taking advantage of the implementation of the effective vertices described in Ref. [37]. We use the VASP suite also for performing semilocal and hybrid-functional calculations. The pseudopotentials used are specified in the Supplemental Material (SM) [55] (see also references [37,41,56–59] therein). The semilocal calculations are based on the exchange-correlation functional proposed by Perdew, Burke, and Ernzerhof (PBE) [60]. The hybrid-functional calculations are carried out with the PBEh(α) functional, in which a fraction α of the semilocal PBE exchange is replaced by Fock exchange [25]. For $\alpha = 0.25$, we denote PBEh(0.25) = PBE0.

B. Scheme for band-offset calculations

In the present paper, we designate with the notation A/B the interface between a material A as overlayer and a material B as substrate. To compute the band offsets of the interface A/B, we use the scheme proposed by Van de Walle and Martin [9] and by Baldereschi *et al.* [11]. In this scheme, the band offsets are obtained through a two-step procedure. In the first step, the band edges of the overlayer A and the substrate B are determined with respect to the local reference level in the respective bulk materials, $E^s_{c/v}$ and $E^o_{c/v}$, where the subscript c refers to the conduction band and the subscript v to the valence band. These energy levels are determined through calculations of bulk materials. It is convenient to take the average electrostatic potential as local reference level, since this level depends on the charge density and is found to converge to constant values at short distances from the interface [9,11,13,19]. In the second step, an interface model structure is considered to extract the line-up of the average electrostatic potential ΔV across the interface. The band offset is then found as

$$\Delta E_{c/v} = E^s_{c/v} - E^o_{c/v} + \Delta V. \tag{8}$$

This scheme is summarized in Fig. 1. The calculations performed in this paper correspond to a temperature of 0 K.

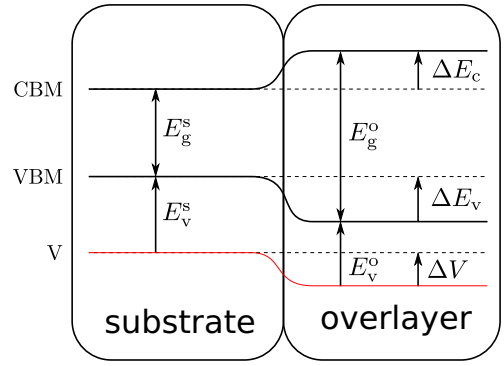

FIG. 1. Scheme of band alignment between substrate and overlayer showing the evolution of the conduction band minimum (CBM) and the valence band maximum (VBM). The red line represents the average electrostatic potential V across the interface. The figure illustrates various quantities defined in text. For the represented case, the signs of ΔV, ΔE_c, and ΔE_v are taken to be positive. When the alignment is such that an arrow points into the opposite direction, we use a negative value for the corresponding physical quantity.

Various electronic-structure methods are investigated in the present paper, including PBE, PBE0, qsGW, qs$G\tilde{W}^{Boot}$, qs$G\tilde{W}^{NQ}$, qs$G\tilde{W}^{LR}$, and qs$G\hat{W}$. In principle, the same electronic-structure method should be used in the bulk and interface calculations. However, since the average electrostatic potential is found to be rather robust upon varying the electronic-structure scheme [13,15,18], it is possible to devise mixed schemes. For instance, when band offsets are obtained at the *GW* level, the line-up potential is often taken from semilocal calculations [14–16,18,41,42,45]. Similarly, the scheme proposed by Alkauskas *et al.* relies on the use of different hybrid functionals for each interface component in order to reproduce their respective band gaps [13]. This is achieved by setting suitable values of Fock exchange α for each bulk component (α^A and α^B). The calculation of the line-up potential is then carried out with the functional PBEh($\bar{\alpha}$), where $\bar{\alpha} = \frac{1}{2}(\alpha^A + \alpha^B)$. The line-up potential is found to vary linearly with $\bar{\alpha}$ and can thus be derived from two calculations, e.g., with PBE and PBE0 functionals. In

TABLE I. Experimental lattice parameters and Poisson ratios of the interface components considered in this paper. The Poisson ratios (ν) are provided for all materials that occur as overlayer in the considered set of interfaces. The lattice parameters (a_{expt}) correspond to 0 K.

Material	ν	a_{expt} (Å)
AlAs	0.33[a]	5.661[b]
AlP	0.32[c]	5.451[d]
GaAs		5.648[e]
GaP		5.448[e]
Ge	0.25[f]	5.658[g]
Si	0.22[h]	5.430[g]
ZnSe	0.28[i]	5.667[j]
CaF_2	0.26[k]	5.463[l]

[a]Reference [61]; [b]Reference [62]; [c]Reference [63]; [d]Reference [64]; [e]Reference [65]; [f]Reference [66]; [g]Reference [67]; [h]Reference [68]; [i]Reference [69]; [j]Reference [70]; [k]Reference [71]; [l]Reference [72].

practice, the difference between the line-up potentials in PBE and PBE0 is rather small in most cases. In the present calculations, it does not exceed 0.06 eV.

At an epitaxially grown interface, we distinguish the substrate and the overlayer materials. Experimentally, the overlayer material adopts the lattice parameter of the substrate in the directions parallel to the interface. Experimental lattice parameters used in this paper are given in Table I. All the interfaces considered in this paper are close to be lattice matched (see Table II), whereby the lack of detailed knowledge about the interfacial atomic structure is minimized. In the vicinity of the interface, the atomic structures of both interface components undergo structural relaxation. In the direction normal to the interface, the lattice parameter of the substrate corresponds to its bulk value, whereas the overlayer is subject to strain effects. These strain effects determine the experimental value for the lattice parameter of the overlayer in the growth direction $a^{\text{o}}_{\text{strain}}$ (cf. Table II). These lattice parameters can be obtained from the experimental lattice constants and the experimental Poisson ratio (Table I). The z direction is taken to be the growth direction and the lattice parameter in this direction is denoted a_z, while the in-plane lattice parameters are denoted $a_\perp$. Here, we aim to calculate band offsets for

TABLE II. Strain in the overlayer resulting from the lattice mismatch when grown on the indicated substrate. The interface orientation is given. The lattice parameter $a^{\text{o}}_{\text{strain}}$ of the overlayer in the growth direction is determined through the use of the experimental lattice parameters and Poisson ratios (Table I).

Overlayer	Substrate	Direction	Mismatch	$a^{\text{o}}_{\text{strain}}$ (Å)
AlP	GaP	(001)	−0.06%	5.460
AlAs	GaAs	(001)	−0.23%	5.701
Ge	AlAs	(011)	0.05%	5.646
Ge	GaAs	(011)	−0.18%	5.698
Ge	ZnSe	(011)	0.16%	5.622
Si	GaP	(011)	0.33%	5.348
ZnSe	GaAs	(011)	−0.34%	5.735
CaF_2	Si	(111)	−0.61%	5.587

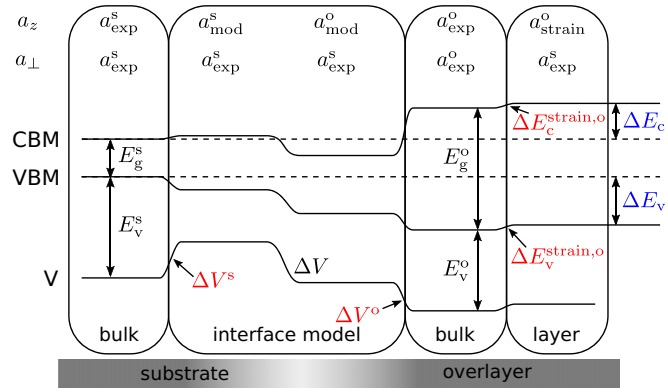

FIG. 2. Scheme for the inclusion of strain effects in the band offset calculation through electronic-structure calculations of ideal bulk structures. The valence band maximum (VBM) and conduction band minimum (CBM) as well as the electrostatic potential V are displayed. From left to right, the scheme involves several systems: the bulk substrate, the model interface, the bulk overlayer, and the strained overlayer. The various ingredients in the calculations are highlighted (red): ΔV^{s}, ΔV^{o}, $\Delta E^{\text{strain,o}}_{\text{c}}$, and $\Delta E^{\text{strain,o}}_{\text{v}}$. For each system, the lattice parameters in the in-plane directions $a_\perp$ and in the growth direction a_z are given. The targeted valence and conduction band offsets are shown (blue).

interface models, which reproduce the experimental atomic structure as well as possible.

To achieve this target, we follow the procedure introduced by Bischoff *et al.* [18], which proposed a method to account for the strain in the overlayer. We model the A/B interface as a superlattice of materials A and B. The in-plane lattice constants are set to the experimental values pertaining to the substrate material B. The atomic structure including the cell parameter in the growth direction are then fully relaxed. By consequence, the lattice parameter of the substrate in this direction differs from its experimental value. Similarly, the lattice parameter of the overlayer in the same direction also differs from its strained value $a^{\text{o}}_{\text{strain}}$. Hence, the strain present in the superlattice originates from two different sources. First, there is a physical effect resulting from the lattice mismatch in the in-plane direction between the two materials at the interface, which causes strain in the overlayer. Second, the structural relaxation in the modeling scheme gives rise to equilibrium lattice parameters ($a^{\text{s}}_{\text{mod}}$ and $a^{\text{o}}_{\text{mod}}$), which differ from their experimental counterparts in both components of the interface (cf. Fig. 2). In the following, we first identify the quantities that are required and then describe their calculation in practical terms. On the side of the substrate, we determine the shift between the electrostatic potentials of the substrate in the interface model and in the bulk at experimental lattice constants, $\Delta V^{\text{s}} = \Delta V(\text{model substrate} \rightarrow \text{bulk substrate})$ (cf. Fig. 2). The band edges of the conduction and valence bands are then determined from a bulk calculation at experimental lattice constants. On the side of the overlayer, we first establish the shift of the electrostatic potential when going from the interface model to the bulk structure at experimental lattice constants $\Delta V^{\text{o}} = \Delta V(\text{model overlayer} \rightarrow \text{bulk overlayer})$ (cf. Fig. 2). We determine the conduction and valence band edges with

TABLE III. Valence and conduction band-offset corrections (in eV) due to strain ($\Delta E_{c/v}^{strain}$), zero-phonon renormalization ($\Delta E_{c/v}^{ZPR}$), and spin-orbit coupling (ΔE_{v}^{SOC}) effects. The strain effects are evaluated at the PBE0 level.

Interface	ΔE_{v}^{strain}	ΔE_{v}^{ZPR}	ΔE_{v}^{SOC}	ΔE_{c}^{strain}	ΔE_{c}^{ZPR}
AlAs/GaAs	−0.13	−0.02	−0.01	−0.09	−0.04
AlP/GaP	−0.01	−0.03	−0.01	0.00	0.00
Ge/AlAs	0.08	−0.02	−0.01	0.10	−0.02
Ge/GaAs	−0.04	0.00	−0.02	0.06	0.02
Ge/ZnSe	0.12	−0.01	−0.04	0.11	0.00
Si/GaP	0.00	0.01	−0.01	0.00	−0.02
ZnSe/GaAs	−0.12	−0.01	0.02	−0.04	−0.01
CaF_2/Si	−0.02	−0.21	−0.01	0.05	−0.06

respect to the electrostatic potential through a bulk calculation of the overlayer material at experimental lattice constants. The final step consists in shifting the band edges to those pertaining to the strained overlayer with lattice parameters corresponding to those of the substrate in the parallel directions and to a_{strain}^{o} in the growth direction. In this way, we obtain $\Delta E_{c/v}^{strain,o} = \Delta E_{c/v}$(bulk overlayer → strained overlayer) (cf. Fig. 2). Gathering all strain contributions for a given interface, we obtain

$$\Delta E_{c/v}^{strain} = \Delta V^{s} + \Delta V^{o} + \Delta E_{c/v}^{strain,o}, \tag{9}$$

which yields the strain corrections for the conduction and valence band offsets. We remark that in principle it is not necessary to transit through the bulk structure of the overlayer at experimental lattice constant. Nevertheless, the consideration of the unconstrained bulk structure of the overlayer allows us to obtain electronic-structure results that can easily be compared with references in the literature. Furthermore, the higher symmetry of the unconstrained structure allows one to keep to a minimum the computational cost of the calculations.

To determine the strain effect on the electrostatic potential and on the band edges in practice, we use the scheme described by Van de Walle [73,74] at the PBE0 level. We set up an interface in which the two components correspond to the same material, but with different lattice constants in the growth direction. The shift of the electrostatic potential can directly be inferred from the line-up across the interface. The shifts of the valence and conduction band edges due to the strain effect are obtained upon aligning the electronic structures of the strained and unstrained materials to the electrostatic potential on either side of the interface. The calculated corrections $\Delta E_{c/v}^{strain}$ are given in Table III, while the individual corrections ΔV^{s}, ΔV^{o}, and $\Delta E_{c/v}^{strain,o}$ are provided in the SM [55]. The total strain corrections in Table III amount to 0.13 eV at most. While these corrections are rather small, they are of the same order as the overall accuracy by which the band offsets are determined and thus need to be included to avoid systematic errors.

The band-edge levels are further corrected for the zero-point renormalization (ZPR) resulting from electron-phonon interactions. For all materials but CaF_2, we use corrections obtained with the nonadiabatic approach from Miglio *et al.* [57]. For CaF_2, we compute the ZPR in the adiabatic approximation using the special displacement method developed by Zacharias and Giustino [58]. For a list of materials including polar compounds, the difference between the two schemes has been found not to exceed 40 meV [57,75], which we consider negligible for the purpose of our study. Using the implementation by Karsai *et al.* [59], we carry out calculations on a 4×4×4 supercell with the PBE functional, which has been found to provide accurate estimates [76]. In this way, we find a ZPR of 0.32 eV for the CaF_2 band gap, corresponding to the largest ZPR value for the materials under consideration. The ZPR corrections applied to the band offsets, ΔE_{v}^{ZPR} and ΔE_{c}^{ZPR} (cf. Table III), are obtained from the difference between the ZPR correction of the two interface components. The latter are provided in the SM [55].

For completeness, we also consider spin-orbit coupling corrections ΔE_{v}^{SOC} on the valence band edges. These corrections for the bulk interface components are given in the SM [55] and their effect amounts to at most 0.04 eV for the interfaces considered in this paper (see Table III). Hence, the band offsets are here corrected for strain, ZPR, and spin-orbit coupling (SOC) effects,

$$\Delta E_{c/v} = \Delta E_{c/v}^{mod} + \Delta E_{c/v}^{strain} + \Delta E_{c/v}^{ZPR} + \Delta E_{c/v}^{SOC}, \tag{10}$$

where $\Delta E_{c/v}^{mod}$ are the bare band offsets obtained for the model interfaces neglecting all strain and ZPR corrections. The corrections ΔE_{c}^{SOC} are neglected.

The main ingredients in our calculations are (i) the band structures of the bulk interface components and (ii) the line-up potential. Point (i) is strongly dependent on the electronic structure scheme and a variety of such schemes are taken under consideration in this paper, including qs*GW* calculations with effective vertex functions. At variance, point (ii) is a very robust quantity and depends only weakly on the electronic structure method, as is seen in Sec. IV. Hence, the main outcome of our paper is establishing the dependence of the band offsets on the electronic structure method used for the band structures of the interface components. In addition, we consider three corrections to account for strain, zero-phonon renormalization, and spin-orbit coupling effects (Table III). However, all these corrections are rather small for the present interfaces and variations resulting from the applied electronic-structure method can be ignored.

TABLE IV. Convergence parameters used in the self-consistent *GW* calculations. N_ω is the number of frequencies sampled on the real axis in the contour-deformation technique, N_{bands} is the number of considered bands, and $N_{\text{sc-bands}}$ is the number of self-consistently updated bands. For all materials, the energy cutoffs for the wave functions and for the response function are set to 500 eV and 333 eV, respectively.

Material	N_ω	N_{bands}	$N_{\text{sc-bands}}$
AlAs	200	1024	112
AlP	200	1024	56
GaAs	150	1152	352
GaP	150	1024	112
Ge	150	1152	64
Si	200	1024	64
ZnSe	150	1152	224
CaF_2	150	500	256

III. BAND GAPS

In this section, we determine the band gaps and the band edges of the bulk materials. The PBE and the PBE0 calculations are performed with 6×6×6 **k**-point grids, which are found to be sufficient for all materials, except for silicon. In the latter case, we use a 12×12×12 **k**-point grid to describe the conduction band minimum, which is not located at a high-symmetry point, but along a symmetry line. In the self-consistent *GW* calculations, we use the convergence parameters given in Table IV. When referring to the same materials, the present convergence parameters agree with settings of a previous paper [49]. The initial electron wave functions and single-particle energies are computed using the PBE functional for all materials, except for germanium for which we use the PBE0 functional due to the vanishingly small PBE band gap. The contour-deformation technique is used in order to perform the energy integration [83]. All the self-consistent *GW* calculations are carried out with 6×6×6 **k**-point grids. For the silicon band gap, we include a correction of 0.15 eV, which is estimated from the difference between G_0W_0 calculations computed with 6×6×6 and 10×10×10 **k**-point grids. All the self-consistent *GW* calculations are further corrected to account for extrapolation to infinite basis set, as described in Refs. [41,84]. In the specific case of qs$G\hat{W}$, we follow the procedure described in Ref. [49]. In particular, we study the convergence behavior of the individual quasiparticle energy levels for the valence and conduction band edges, which is generally more accurate than just focusing on the band gap (e.g., see Ref. [85]). The extrapolated corrections for the band edges are given in the SM [55]. The largest corrections are found for CaF_2, for which they range up to 0.60 eV. For the semiconductors, the largest corrections amount to 0.25 eV (see SM [55]).

The band gaps obtained with the various electronic-structure schemes considered in this paper are shown in Table V along with experimental values for comparison. The experimental results for the semiconductors all correspond to very low temperatures and can directly be compared with the theoretical results corresponding to 0 K. In the case of CaF_2, the measurement has been made at 90 K, but from a linear extrapolation of the temperature dependent data in Ref. [82] to 0 K we estimate a band-gap increase of only 0.07 eV. The accuracy of the various schemes can be estimated by separately determining with respect to the experimental values the mean absolute error (MAE) for the narrow-band semiconductors and the absolute error (AE) for CaF_2. It is preferable to distinguish these two cases due the large band-gap difference. Due to its well-known band-gap underestimation, the PBE functional shows the largest errors with a MAE of 1.04 eV for the semiconductors and an AE of 4.8 eV for CaF_2. A significant reduction of the MAE to 0.35 eV is achieved with PBE0, even though the band gaps remain systematically overestimated. At variance, for CaF_2, the PBE0 band

TABLE V. Fundamental band gaps of bulk materials calculated with various electronic-structure schemes at a temperature of 0 K. The calculated band gaps include ZPR and SOC corrections (cf. SM [55]). The experimental lattice constants given in Table I are used. We separately determine with respect to the experimental values the mean absolute error (MAE) for the narrow-band semiconductors and the absolute error (AE) for CaF_2. The qs$G\tilde{W}^{\text{Boot}}$ and qs$G\tilde{W}^{\text{NQ}}$ results for all materials are taken from Ref. [37], except those for Ge and CaF_2, which have been obtained here for the scope of this paper.

Material	PBE	PBE0	qs*GW*	qs$G\tilde{W}^{\text{Boot}}$	qs$G\tilde{W}^{\text{NQ}}$	qs$G\tilde{W}^{\text{LR}}$	qs$G\hat{W}$	Expt.
AlAs	1.25	2.54	2.56	2.33	2.22	2.39	2.25	2.24[a]
AlP	1.45	2.82	2.84	2.61	2.48	2.63	2.51	2.52[a]
GaAs	0.40	1.83	1.70	1.54	1.59	1.54	1.38	1.52[a]
GaP	1.49	2.82	2.62	2.44	2.66	2.42	2.33	2.35[a]
Ge	0.00	1.22	1.02	0.95	0.92	0.87	0.85	0.74[b]
Si	0.49	1.70	1.34	1.23	1.17	1.19	1.17	1.17[c]
ZnSe	1.10	2.88	3.22	2.84	2.86	3.00	2.78	2.82[d]
MAE	1.04	0.35	0.28	0.08	0.09	0.10	0.05	
CaF_2	6.96	9.79	13.39	12.02	12.35	13.28	12.64	11.8[e]
AE	4.8	2.0	1.6	0.2	0.6	1.5	0.9	

[a]Reference [77], extrapolated to $T = 0$ K.
[b]Reference [78], extrapolated to $T = 0$ K.
[c]Reference [79], extrapolated to $T = 0$ K.
[d]Reference [80], obtained at $T = 6$ K.
[e]Reference [81], inferred from the 12.1 eV direct transition measured at $T = 90$ K in Ref. [82].

TABLE VI. Valence band-edge levels (in eV) of bulk materials with respect to the average electrostatic potential, as obtained from the various electronic-structure schemes considered in this paper. Strain, ZPR, and SOC effects are not included, since they do not affect the comparison. For PBEh(α), the value of α reproducing the band gap is shown in parentheses. The qs$G\tilde{W}^{\mathrm{Boot}}$ and qs$G\tilde{W}^{\mathrm{NQ}}$ results are taken from Ref. [37] for all materials, except for Ge and CaF_2 for which they have been obtained here for the scope of this paper.

Material	PBE	PBE0	PBEh(α)	qsGW	qs$G\tilde{W}^{\mathrm{Boot}}$	qs$G\tilde{W}^{\mathrm{NQ}}$	qs$G\tilde{W}^{\mathrm{LR}}$	qs$G\hat{W}$
AlAs	2.89	2.12	2.30 (0.19)	1.54	1.49	1.58	1.61	2.34
AlP	4.20	3.37	3.55 (0.20)	2.87	2.84	2.92	2.94	3.65
GaAs	3.07	2.37	2.52 (0.20)	1.91	1.86	1.88	1.95	2.57
GaP	4.37	3.61	3.88 (0.16)	3.16	3.16	2.92	3.21	3.88
Ge	3.10	2.33	2.61 (0.16)	1.84	1.73	1.88	1.89	2.53
Si	2.72	2.07	2.36 (0.14)	1.73	1.69	1.74	1.76	2.32
ZnSe	2.51	1.50	1.53 (0.24)	0.74	0.77	0.77	0.83	1.44
CaF_2	1.03	−1.01	−2.44 (0.43)	−3.95	−3.25	−3.41	−4.09	−2.88

gap underestimates the experimental value by ∼2 eV. These results are in accord with general tendencies of PBE0 for narrow and wide band-gap materials [86]. With qsGW, we find band gaps showing slightly smaller MAE and AE of 0.28 and 1.6 eV, respectively. This error results from an overall overestimation of the experimental band gaps by ∼20%, in accord with previous results in the literature [32,33,35–37].

To reduce these deviations it is necessary to include vertex corrections, which approximately account for electron-hole interactions in the polarizability [35–37,40,41]. For the semiconductors, qs$G\tilde{W}^{\mathrm{Boot}}$, qs$G\tilde{W}^{\mathrm{NQ}}$, and qs$G\tilde{W}^{\mathrm{LR}}$ indeed yield smaller MAEs of 0.08, 0.09, and 0.10 eV, respectively. In particular, we remark that for this set of semiconductors the effective vertex functions yield an accuracy similar to that achieved with the NANOQUANTA vertex. Furthermore, the achieved MAE values are noticeably smaller than obtained with the same schemes in Ref. [37], where they are found to range between 0.14 and 0.36 eV for a larger set of materials. When the vertex function is also included in the self-energy as in qs$G\hat{W}$, the MAE further drops to 0.05 eV. In particular, when compared to qs$G\tilde{W}^{\mathrm{LR}}$, qs$G\hat{W}$ leads to a systematic further reduction of the band gap (cf. Table V). We note that for the narrow band-gap materials the self-consistent GW schemes including vertex corrections give band gaps in close agreement with experiment, i.e., within at most ∼0.3 eV. It is worth mentioning that the inclusion of ZPR corrections (cf. SM [55]) reduces the MAE of all electronic-structure schemes by ∼0.05 eV, indicating that these corrections contribute to improving the agreement with the experimental values. The results for qs$G\tilde{W}^{\mathrm{LR}}$ and qs$G\hat{W}$ for these materials are also in good agreement with previous self-consistent GW calculations based on a second-order expansion of Γ in W [41].

For the wide band-gap material CaF_2, the various self-consistent GW schemes including vertex corrections give band gaps differing by more than 1 eV among each other. Since these GW schemes correspond to the present state of the art, this suggests that a large indetermination still subsists in the case of predictions for a large band-gap material such as CaF_2. For this material, the band gap is found to correlate with the high-frequency dielectric constant ε_∞ in a sensitive way. We find ε_∞ of 1.71, 2.15, 1.99, 1.82, and 1.91 for qs$G\tilde{W}^{\mathrm{Boot}}$, qs$G\tilde{W}^{\mathrm{NQ}}$, qs$G\tilde{W}^{\mathrm{LR}}$, and qs$G\hat{W}$, to be compared with the experimental value of 2.045 [87]. The best description of ε_∞ is found for qs$G\tilde{W}^{\mathrm{Boot}}$ and qs$G\tilde{W}^{\mathrm{NQ}}$, which also yield the most accurate band gaps. In a previous calculation at the qs$G\tilde{W}^{\mathrm{Boot}}$ level, Bischoff *et al.* found a band gap of 11.47 eV [18] to be compared with our value of 12.29 eV obtained within the same theoretical scheme (without including ZPR and SOC corrections). This difference of about 0.9 eV should solely be assigned to the use of different computational setups in the two cases. At the one-shot G_0W_0 level, Ma and Rohlfing yielded a band gap of 11.5 eV [88].

We give in Table VI the valence band-edge levels of the materials studied with respect to the average electrostatic potential for the various electronic-structure schemes. As we will see in the next section, the average electrostatic potential is robust among the electronic-structure schemes investigated in this paper. Hence, it is meaningful to compare the relative positions of the valence band edges across the involved schemes. In addition to the schemes considered so far, we provide results for PBEh(α) with α set to reproduce the experimental band gap, since this scheme has empirically been found to provide accurate energy-level alignments [13,18,32,42,43]. All the self-consistent GW schemes except qs$G\hat{W}$ systematically set the valence band edge at lower energy compared to the PBE0 and PBEh(α) calculations. When the vertex is included in the polarizability, as in the qs$G\tilde{W}$ schemes, the valence band edge is generally found to undergo only a small shift compared to qsGW, while the band gaps generally undergo a reduction of larger size (cf. Table V). The inclusion of the short-range part of the vertex in qs$G\hat{W}$ moves up the valence band edge level with respect to the qs$G\tilde{W}$ values, bringing them closer to the PBEh(α) levels. Indeed, in this case, the shift of the valence band edge is generally much larger than the effect on the band gap (cf. Table V). In short, the qs$G\tilde{W}$ calculations provide similar valence band-edge levels, while qs$G\hat{W}$ displaces these levels to higher energies.

IV. BAND ALIGNMENT

To calculate the line-up potential, it is necessary to set up atomistic models of the interfaces. In this paper, we only consider lattice-matched interfaces to simplify the construction of model structures representing the interfacial atomic arrangement. The semiconductor-semiconductor model interfaces are generated from an initial structure in which the two interface

components are stacked in a superlattice geometry along the growth direction. For the interfaces grown along the (001) direction, we use a simulation cell with eight atomic layers for each component with two atoms per layer. For the interfaces grown along the (011) direction, we take seven layers for each component with two atoms per layer. The in-plane lattice parameter is set to the experimental value of the substrate in all cases. The atomic structure and the cell size in the growth direction are fully relaxed with the PBE functional. The structural model for the CaF_2/Si interface corresponds to the T_4 interface model in the B-type orientation [89,90], where Si-Ca bonds predominate at the interface. The silicon component contains fourteen layers, while the CaF_2 component consists of six layers of Ca and ten layers of F. We here adopt the model structure provided in Ref. [91], which was generated through a scheme analogous to the one employed in the present paper [18]. The convergence parameters of the electronic-structure calculations are set to achieve an accuracy of 10 meV or lower in the potential line-up. Depending on the interface, this required **k**-point grids up to 8×8 in the in-plane directions, up to 5 **k** points in the growth direction, and an energy cut-off up to 1000 eV (see details in SM [55]). From the relaxed structures, we determine the model lattice parameters of the substrate and overlayer ($a^{\mathrm{s}}_{\mathrm{mod}}$ and $a^{\mathrm{o}}_{\mathrm{mod}}$, cf. Fig. 2) by considering the interatomic layer spacing at the center of each superlattice component. These lattice parameters are then used to determine strain corrections (see Sec. II B).

The electrostatic Hartree potential along the growth direction is obtained through an average over the in-plane directions. The potential obtained in this way is then convoluted with a Gaussian function to achieve the average macroscopic electrostatic potential. This potential assumes constant levels in the central regions of the two interface components. The line-up potential ΔV is then defined as the difference between these two potential levels. The Gaussian broadening is chosen such that the oscillations are smoothed without affecting the average values [92]. We remark that the adopted procedure for the determination of the potential line-up relies on the fact that the potential assumes constant values away from the interface region. Indeed, in our models, we do not observe any charge transfer between the various interfaces resulting in flat potentials between the interfaces, very similar to those found in Refs. [15,18] to which we refer to as examples. In more realistic interfaces, the occurrence of defect states gives rise to charge traps that produce band-bending effects [93]. Such effects occur on long-range length scales and are quite distinct with respect to band offsets, which occur on atomic-scale distances.

After setting up the interfaces, the calculation of the line-up potential is carried out with both the PBE and PBE0 functionals. The results are reported in Table VII. The PBE and PBE0 values are in excellent agreement with each other, with a difference lower than 60 meV in the worst case, corresponding to CaF_2/Si. This indicates that the potential line-up is robust when going from PBE to PBE0, in accord with previous findings [13,15].

It is of interest to verify whether the robustness of the line-up potential observed for semilocal and hybrid functionals also holds for the self-consistent *GW* calculations. Indeed, in such calculations, the effects of self-consistently updating the density has only rarely been considered at interfaces [14]. Due to their high computational cost, we perform qs$G\hat{W}$ calculations of the line-up potential only at one semiconductor-semiconductor interface (AlP/GaP) and one insulator-semiconductor interface (CaF_2/Si). The resulting line-up potentials are given in Table VII, for comparison with the semilocal and hybrid-functional results. We find that all line-up potentials are very close to each other, with differences amounting to at most 90 meV. Hence, our results confirm that the self-consistent update of the density in self-consistent *GW* calculations only lead to minor effects, as found previously for the SiO_2/Si interface [14]. This supports the common practice of determining the line-up potential through semilocal or hybrid functional calculations.

TABLE VII. Line-up potential ΔV (in eV) as calculated in PBE, PBE0, and qs$G\hat{W}$ for the interfaces considered in this paper. Given the high computational cost, the qs$G\hat{W}$ calculations have been performed only for two interfaces.

Interface	ΔV_{PBE}	ΔV_{PBE0}	$\Delta V_{\mathrm{qs}G\hat{W}}$
AlP/GaP	0.33	0.33	0.36
AlAs/GaAs	0.35	0.35	
Ge/AlAs	−1.04	−1.06	
Ge/GaAs	−0.60	−0.63	
Ge/ZnSe	−0.82	−0.85	
Si/GaP	−1.90	−1.89	
ZnSe/GaAs	0.20	0.19	
CaF_2/Si	3.97	4.03	4.06

We now have all the ingredients to determine the band offsets for the interfaces considered here. The band offsets are calculated with Eq. (10) including strain, ZPR, and SOC corrections for all the electronic-structure schemes considered in this paper, namely PBE, PBE0, PBEh(α), qsGW, qs$G\tilde{W}^{\mathrm{Boot}}$, qs$G\tilde{W}^{\mathrm{NQ}}$, qs$G\tilde{W}^{\mathrm{LR}}$, and qs$G\hat{W}$. Here, the PBEh($\alpha$) scheme refers to calculations in which we use PBEh(α) functionals with α set to reproduce the experimental band gap in each interface component and the PBEh($\bar{\alpha}$) functional for the determination of the line-up potential in the interface model (cf. Sec. II B). When matching the experimental band gap, we ensure that the ZPR and SOC corrections are properly accounted for. Valence and conduction band offsets are given in Tables VIII and IX, respectively. For the PBE results, the line-up potential is taken at the PBE level. For all other schemes, the line-up potential obtained with PBE0 is used.

Rather than discussing valence and conduction band offsets separately, we focus for each electronic-structure scheme on the MAEs obtained for all band offsets taken together (cf. Table X). Rather than aiming at a statistically meaningful analysis, which is prevented by the small number of interfaces, we use the MAE values to guide the comparison with experiment. We first discuss the set of semiconductor heterostructures, because the large errors occurring in the case of the CaF_2/Si interface might otherwise obscure general trends. The PBE functional yields the largest errors in the band gaps and correspondingly the largest errors in the band offsets. Surprisingly, despite its inherent errors in the description of the band gaps, PBE0 achieves an accuracy similar to that of

TABLE VIII. Valence band offset ΔE_v (in eV) at a temperature of 0 K, as calculated with the various electronic-structure schemes considered in this paper, compared to experimental values. We separately determine with respect to the experimental values the mean absolute error (MAE) for the semiconductor-semiconductor interfaces and the absolute error (AE) for the CaF_2/Si interface.

Interface	PBE	PBE0	PBEh(α)	qsGW	qs$G\tilde{W}^{\mathrm{Boot}}$	qs$G\tilde{W}^{\mathrm{NQ}}$	qs$G\tilde{W}^{\mathrm{LR}}$	qs$G\hat{W}$	Expt.
AlP/GaP	0.48	0.54	0.64	0.61	0.64	0.30	0.58	0.55	0.56[a]
AlAs/GaAs	0.40	0.47	0.44	0.58	0.58	0.51	0.55	0.45	0.53[b]
Ge/AlAs	−1.16	−1.16	−1.26	−1.25	−1.19	−1.25	−1.23	−1.14	−0.95[c]
Ge/GaAs	−0.56	−0.60	−0.70	−0.57	−0.51	−0.63	−0.57	−0.59	−0.56[d]
Ge/ZnSe	−1.24	−1.50	−1.74	−1.77	−1.63	−1.78	−1.72	−1.75	−1.52[e]
Si/GaP	−0.28	−0.35	−0.38	−0.45	−0.42	−0.70	−0.43	−0.32	−0.80[f]
ZnSe/GaAs	0.64	0.92	1.04	1.22	1.13	1.16	1.16	1.18	1.10[g]
MAE	0.24	0.14	0.19	0.16	0.13	0.15	0.14	0.16	
CaF_2/Si	5.46	6.88	8.62	9.49	8.75	8.95	9.66	9.00	8.7[h]
AE	3.2	1.8	0.1	0.8	0.1	0.3	1.0	0.3	

[a]Reference [94]; [b]Reference [77]; [c]Reference [95]; [d]Reference [96]; [e]Reference [97]; [f]Reference [98]; [g]Reference [97]; [h]References [99–101].

PBEh(α), on the order of 0.2 eV. Similarly, all *GW* schemes yield MAEs of 0.2 eV or lower. The calculated MAEs do not correlate with the average error by which the considered scheme yields band gaps (see δE_g in Table X). In fact, the band offsets in some *GW* schemes are described even more accurately than in PBEh(α), which reproduces the experimental band gap by construction. This suggests that the specific values of the calculated MAEs ranging between 0.14 and 0.20 eV do not carry particular significance. Furthermore, it should be remarked that the MAEs achieved here for the band offsets are significantly lower than found for ionization potentials in Ref. [37], where, MAEs between 0.3 and 0.8 eV were found, depending on the employed *GW* scheme. This further suggests that the present errors in the range 0.14–0.20 eV might result from error cancellation due to the similar nature of the interface components in the set of lattice-matched interfaces considered here [16]. In addition, we remark that the NANOQUANTA vertex does not yield a higher accuracy for the band offsets than the effective vertices, suggesting that it is not worth performing computationally more expensive qs$G\tilde{W}^{\mathrm{NQ}}$ calculations for this type of semiconductor interfaces. Similarly, the qs$G\hat{W}$ scheme, which had been designed to improve absolute energy-level alignments [37] does not stand out for higher accuracy compared to the other self-consistent *GW* schemes. The generally low MAE values recorded for all *GW* schemes investigated here are even more striking when one considers that the experimental values might not correspond to abrupt interfaces as assumed in the present paper. For instance, previous research has shown that the discrepancy between experimental and theoretical predictions in the case of the Si/GaP interface could be explained by allowing for atomic interlayer diffusion at the interface [102].

In a previous study, Steiner *et al.* achieved valence band offsets calculated with PBE, PBE0, and PBEh(α) for the same set of semiconductor-semiconductor interfaces, yielding respective MAEs of 0.16, 0.12, and 0.22 eV [15]. However, these calculations did not include relaxation, strain, ZPR, or spin-orbit coupling effects. Compared with our results, we record a deterioration of the accuracy of PBE and PBE0, but an improvement for PBEh(α) (see Table VIII). Hinuma *et al.* also investigated the valence band offsets at the same semiconductor heterostructures considered here [16]. The PBE band offsets are within 0.05 eV from our results except those for interfaces containing Ge, which show discrepancies between 0.2 and 0.3 eV likely due to a different treatment of Ge [16]. Hinuma *et al.* also carried out *GW* calculations, but with different schemes than those considered here, resulting in differences on the order of 0.1–0.2 eV for

TABLE IX. Conduction band offset ΔE_c (in eV) at a temperature of 0 K, as calculated with the various electronic-structure schemes considered in this paper, compared to experimental values. The experimental values are inferred from the valence band offset and the experimental band gaps. We separately determine with respect to the experimental values the mean absolute error (MAE) for the semiconductor-semiconductor interfaces and the absolute error (AE) for the CaF_2/Si interface.

Interface	PBE	PBE0	PBEh(α)	qsGW	qs$G\tilde{W}^{\mathrm{Boot}}$	qs$G\tilde{W}^{\mathrm{NQ}}$	qs$G\tilde{W}^{\mathrm{LR}}$	qs$G\hat{W}$	Expt.
AlP/GaP	−0.53	−0.56	−0.47	−0.39	−0.48	−0.48	−0.38	−0.37	−0.39
AlAs/GaAs	0.43	0.21	0.25	0.24	0.17	0.08	0.25	0.39	0.19
Ge/AlAs	−0.19	−0.18	−0.25	−0.29	−0.20	−0.06	−0.30	−0.27	−0.55
Ge/GaAs	0.10	−0.10	−0.14	−0.17	−0.15	−0.10	−0.17	−0.01	−0.22
Ge/ZnSe	0.07	−0.15	−0.33	−0.39	−0.23	−0.13	−0.38	−0.14	−0.56
Si/GaP	−0.82	−0.78	−0.85	−0.83	−0.81	−0.79	−0.81	−0.84	−0.38
ZnSe/GaAs	0.02	0.06	0.19	0.23	0.09	0.04	0.22	0.15	0.20
MAE	0.33	0.23	0.18	0.14	0.20	0.26	0.14	0.24	
CaF_2/Si	0.94	1.14	1.96	2.49	1.98	2.15	2.36	2.40	1.93
AE	1.0	0.8	0.0	0.6	0.1	0.2	0.4	0.5	

TABLE X. Mean absolute errors (MAE) (in eV) calculated with respect to experimental values for band offsets ($\delta\Delta E_{c/v}$). The conduction and valence band offsets are considered together. For the semiconductor-semiconductor interfaces (Semi-Semi), we also give the MAE of the semiconductor band gaps (δE_g). For the CaF_2/Si interface, δE_g represents the deviation of the band gap of CaF_2 from the experimental value.

	Semi-Semi		CaF_2/Si	
Scheme	δE_g	$\delta\Delta E_{c/v}$	δE_g	$\delta\Delta E_{c/v}$
PBE	1.04	0.29	4.8	2.1
PBE0	0.35	0.19	2.0	1.3
PBEh(α)	0	0.19	0.0	0.1
qsGW	0.28	0.15	1.6	0.7
qs$G\tilde{W}^{\text{Boot}}$	0.08	0.17	0.2	0.1
qs$G\tilde{W}^{\text{NQ}}$	0.09	0.20	0.6	0.2
qs$G\tilde{W}^{\text{LR}}$	0.10	0.14	1.5	0.7
qs$G\hat{W}$	0.05	0.20	0.9	0.4

individual band offsets. More specifically, they carried out GW_0, $GW^{\text{TC-TC}}$, and $GW\Gamma^1$ calculations finding respective MAEs of 0.12, 0.16, and 0.15 eV, when evaluated on the same set of semiconductor heterostructures as studied in this paper. This range of values is consistent with our results (0.13–0.16 eV, see Table VIII), further confirming that GW calculations for this set of interfaces generally yield an accurate description.

For the CaF_2/Si interface, the largest errors are obtained with PBE and PBE0, reflecting the errors found with these schemes in the description of the band gap (see δE_g in Table X). In PBEh(α), the experimental band gaps of the interface components are reproduced by construction and the calculated band offsets are found to closely match their experimental counterparts, in accord with the good energy-level alignments previously observed for this functional [13,18,32,42,43]. The GW schemes yield MAEs for the band offsets ranging between 0.1 and 0.7 eV. The worse result is found for qsGW and qs$G\tilde{W}^{\text{LR}}$, while the best result is obtained with qs$G\tilde{W}^{\text{Boot}}$. In the latter case, the deviations with respect to the experimental band offsets are on par with the PBEh(α) functional. The qs$G\tilde{W}^{\text{NQ}}$ closely follows with a MAE of 0.2 eV. The qs$G\hat{W}$ scheme deceptively yields a higher MAE of 0.4 eV, although not inconsistent with its expected accuracy of 0.3 eV in reproducing absolute energy levels [37]. More generally, the errors are found to correlate with the accuracy by which the GW schemes describe the band gap of CaF_2 (cf. Table X). For this interface, the spread in the GW band offsets is rather large. Like in the case of the semiconductor-semiconductor interfaces, it should be mentioned that the experimental band offsets of the CaF_2/Si interface are also subject to some indetermination. Indeed, they are highly sensitive to the fraction of interfacial Si-F bonding [18], with valence-band offsets varying between 7 [103,104] and 8.8 eV [100]. The values adopted in Tables VIII and IX result from an average over various experimental values corresponding to samples with a low fraction of interfacial Si-F bonding [99–101].

V. CONCLUSIONS

In this paper, we investigate energy-level alignments calculated through advanced GW schemes including effective vertex corrections by focusing on lattice-matched interfaces. The considered set of interfaces comprise seven semiconductor-semiconductor interfaces and one insulator-semiconductor interface. For each interface considered, we set up an atomic model structure in the superlattice geometry and allow for full structural relaxation starting from the ideally abrupt interface. Our study includes a panel of GW schemes, including qsGW, qs$G\tilde{W}^{\text{Boot}}$, qs$G\tilde{W}^{\text{NQ}}$, qs$G\tilde{W}^{\text{LR}}$, and qs$G\hat{W}$. These schemes differ in the way vertex corrections are accounted for. The qsGW scheme does not carry any vertex corrections and leads to band gaps overestimated by 20%. Improved band gaps are obtained when vertex corrections are included. We consider three schemes (qs$G\tilde{W}^{\text{Boot}}$, qs$G\tilde{W}^{\text{NQ}}$, and qs$G\tilde{W}^{\text{LR}}$) in which a vertex function enters the polarizability and one scheme (qs$G\hat{W}$) in which a vertex function is included in both the polarizability and the self-energy. For all these schemes, we determine valence and conduction band offsets through the method based on the line-up of the average electrostatic potential. We take care of properly including strain, zero-point renormalization, and spin-orbit corrections to avoid any systematic bias.

First, our study focuses on the band gaps of the involved bulk materials. The band gaps of the semiconductors are reproduced with high accuracy as characterized by mean absolute errors in the range between 0.05 and 0.10 eV, with the best result obtained for qs$G\hat{W}$. For the insulator CaF_2, the accuracy of the GW schemes is found to deteriorate, with deviations with respect to the experimental value reaching up to 1.5 eV, even when considering only GW schemes including vertex corrections. In particular, these GW schemes yield band gaps spread over a range larger than 1 eV, suggesting that the predictive potential of such state-of-the-art schemes is severely challenged when considering a wide band-gap material, such as CaF_2. Nevertheless, the band gap calculated with qs$G\tilde{W}^{\text{Boot}}$ approaches the experimental value within 0.2 eV. Focusing on the valence band maximum relative to the average electrostatic potential, we find that the GW schemes including the vertex function in the polarizability give results in close agreement with qsGW, indicating that the band-gap differences primarily result from shifts of the conduction band edge. At variance, the qs$G\hat{W}$ scheme leads to an overall upwards shift of the valence band edge, while affecting the band gap in a minor fashion.

Our study devotes particular attention to the potential line-up as calculated for the model interfaces. Our results support that the line-up potential is particularly robust showing only minor variations when different electronic-structure schemes are employed. This property does not only hold when comparing semilocal and hybrid functional results, but also when including GW calculations in which the charge density is self-consistently iterated. The largest difference recorded for the interfaces considered in this work amounts to only 90 meV.

Next, our analysis focuses on the band offsets. For the semiconductor heterostructures, we find that all the self-consistent GW schemes yield mean absolute errors of 0.2 eV or lower. The observed errors do not appear to correlate with

the accuracy by which the band gaps are described, indicating that the specific error of each electronic structure scheme is not informative. While this level of accuracy is higher than the smallest average error achieved for absolute energy-level alignments in the literature, this result does not allow us to discriminate between the various considered schemes. For the insulator-semiconductor interface, the observed errors on the band offsets are larger, ranging up to 0.7 eV when considering the various *GW* schemes. In the case of the CaF_2/Si interface and unlike for the semiconductor interfaces, the error on the band offsets for a given *GW* scheme strongly correlates with the accuracy by which that same scheme reproduces the band gap of the insulator material. In particular, the qs$G\tilde{W}^{\mathrm{Boot}}$ scheme, which has been found to best describe the insulator band gap, yields band offsets within a remarkable accuracy of 0.1 eV. Further investigations including a large set of insulator-semiconductor interfaces are necessary to assess whether the observed trends hold more generally.

In this paper, we investigate band offsets at lattice-matched interfaces with the scope of benchmarking energy-level alignments in a context alternative to that of ionization potentials at surfaces. This study has revealed that semiconductor-semiconductor interfaces do not allow one to critically confront competing state-of-the-art many-body perturbation methods. Therefore, insulator-semiconductor interfaces spanning larger band offsets are expected to constitute a better benchmark set for investigating energy-level alignments at interfaces. However, in the study of the CaF_2/Si interface, we found that the considered *GW* schemes differ significantly in describing the large band gap of the insulator, thereby preventing us from extracting meaningful considerations from the calculated band offsets. For the wide band-gap material studied here, the accurate reproduction of the band gap by current state-of-the-art electronic structure schemes appears thus as an open problem, which should be addressed before returning to the alignment issue.

ACKNOWLEDGMENTS

This work is supported by Grant No. 200020-152799 of the Swiss National Science Foundation (SNSF). The calculations were performed at the Swiss National Supercomputing Center (CSCS) under Project ID No. s1122 and at SCITAS-EPFL.

[1] A. Franciosi and C. G. Van de Walle, Heterojunction band offset engineering, Surf. Sci. Rep. **25**, 1 (1996).
[2] E. Assmann, P. Blaha, R. Laskowski, K. Held, S. Okamoto, and G. Sangiovanni, Oxide heterostructures for efficient solar cells, Phys. Rev. Lett. **110**, 078701 (2013).
[3] L. Etgar, P. Gao, Z. Xue, Q. Peng, A. K. Chandiran, B. Liu, Md. K. Nazeeruddin, and M. Grätzel, Mesoscopic $CH_3NH_3PbI_3/TiO_2$ heterojunction solar cells, J. Am. Chem. Soc. **134**, 17396 (2012).
[4] M. Grätzel, Dye-sensitized solid-state heterojunction solar cells, MRS Bull. **30**, 23 (2005).
[5] Q. Zhao, A. Hazarika, X. Chen, S. P. Harvey, B. W. Larson, G. R. Teeter, J. Liu, T. Song, C. Xiao, L. Shaw *et al.*, High efficiency perovskite quantum dot solar cells with charge separating heterostructure, Nat. Commun. **10**, 2842 (2019).
[6] G. Di Liberto, L. Cipriano, S. Tosoni, and G. Pacchioni, Rational design of semiconductor heterojunctions for photocatalysis, Chem. A Eur. J. **27**, 13306 (2021).
[7] T. Nishimura, Understanding and controlling band alignment at the metal/germanium interface for future electric devices, Electronics **11**, 2419 (2022).
[8] G.-S. Kim, S.-H. Kim, J. Park, K. Han, J. Kim, and H.-Y. Yu, Schottky barrier height engineering for electrical contacts of multilayered MoS_2 transistors with reduction of metal-induced gap states, ACS Nano **12**, 6292 (2018).
[9] C. G. Van de Walle and R. M. Martin, Theoretical calculations of semiconductor heterojunction discontinuities, J. Vac. Sci. Technol. B **4**, 1055 (1986).
[10] C. G. Van de Walle and R. M. Martin, Theoretical study of band offsets at semiconductor interfaces, Phys. Rev. B **35**, 8154 (1987).
[11] A. Baldereschi, S. Baroni, and R. Resta, Band offsets in lattice-matched heterojunctions: A model and first-principles calculations for GaAs/AlAs, Phys. Rev. Lett. **61**, 734 (1988).
[12] M. Peressi, N. Binggeli, and A. Baldereschi, Band engineering at interfaces: Theory and numerical experiments, J. Phys. D: Appl. Phys. **31**, 1273 (1998).
[13] A. Alkauskas, P. Broqvist, F. Devynck, and A. Pasquarello, Band offsets at semiconductor-oxide interfaces from hybrid density-functional calculations, Phys. Rev. Lett. **101**, 106802 (2008).
[14] R. Shaltaf, G.-M. Rignanese, X. Gonze, F. Giustino, and A. Pasquarello, Band offsets at the Si/SiO_2 interface from many-body perturbation theory, Phys. Rev. Lett. **100**, 186401 (2008).
[15] K. Steiner, W. Chen, and A. Pasquarello, Band offsets of lattice-matched semiconductor heterojunctions through hybrid functionals and G_0W_0, Phys. Rev. B **89**, 205309 (2014).
[16] Y. Hinuma, A. Grüneis, G. Kresse, and F. Oba, Band alignment of semiconductors from density-functional theory and many-body perturbation theory, Phys. Rev. B **90**, 155405 (2014).
[17] L. Weston, H. Tailor, K. Krishnaswamy, L. Bjaalie, and C. G. Van de Walle, Accurate and efficient band-offset calculations from density functional theory, Comput. Mater. Sci. **151**, 174 (2018).
[18] T. Bischoff, I. Reshetnyak, and A. Pasquarello, Band alignment at the CaF_2/Si(111) interface through advanced electronic structure calculations, Phys. Rev. B **101**, 235302 (2020).
[19] G. D. Liberto and G. Pacchioni, Band offset in semiconductor heterojunctions, J. Phys.: Condens. Matter **33**, 415002 (2021).
[20] P. Hohenberg and W. Kohn, Inhomogeneous electron gas, Phys. Rev. **136**, B864 (1964).
[21] W. Kohn and L. J. Sham, Self-consistent equations including exchange and correlation effects, Phys. Rev. **140**, A1133 (1965).
[22] L. J. Sham and M. Schlüter, Density-functional theory of the energy gap, Phys. Rev. Lett. **51**, 1888 (1983).

[23] J. P. Perdew and M. Levy, Physical content of the exact Kohn-Sham orbital energies: Band gaps and derivative discontinuities, Phys. Rev. Lett. **51**, 1884 (1983).

[24] A. D. Becke, A new mixing of Hartree–Fock and local density-functional theories, J. Chem. Phys. **98**, 1372 (1993).

[25] J. P. Perdew, M. Ernzerhof, and K. Burke, Rationale for mixing exact exchange with density functional approximations, J. Chem. Phys. **105**, 9982 (1996).

[26] J. Heyd, G. E. Scuseria, and M. Ernzerhof, Hybrid functionals based on a screened Coulomb potential, J. Chem. Phys. **118**, 8207 (2003).

[27] F. Devynck, F. Giustino, P. Broqvist, and A. Pasquarello, Structural and electronic properties of an abrupt 4H–SiC(0001)/SiO_2 interface model: Classical molecular dynamics simulations and density functional calculations, Phys. Rev. B **76**, 075351 (2007).

[28] P. Borlido, M. A. L. Marques, and S. Botti, Local hybrid density functional for interfaces, J. Chem. Theory Comput. **14**, 939 (2018).

[29] H. Zheng, M. Govoni, and G. Galli, Dielectric-dependent hybrid functionals for heterogeneous materials, Phys. Rev. Mater. **3**, 073803 (2019).

[30] L. Hedin, New method for calculating the one-particle Green's function with application to the electron-gas problem, Phys. Rev. **139**, A796 (1965).

[31] M. S. Hybertsen and S. G. Louie, Electron correlation in semiconductors and insulators: Band gaps and quasiparticle energies, Phys. Rev. B **34**, 5390 (1986).

[32] W. Chen and A. Pasquarello, Band-edge positions in *GW*: Effects of starting point and self-consistency, Phys. Rev. B **90**, 165133 (2014).

[33] M. van Schilfgaarde, T. Kotani, and S. Faleev, Quasiparticle self-consistent *GW* theory, Phys. Rev. Lett. **96**, 226402 (2006).

[34] T. Kotani, M. van Schilfgaarde, and S. V. Faleev, Quasiparticle self-consistent *GW* method: A basis for the independent-particle approximation, Phys. Rev. B **76**, 165106 (2007).

[35] M. Shishkin, M. Marsman, and G. Kresse, Accurate quasiparticle spectra from self-consistent *GW* calculations with vertex corrections, Phys. Rev. Lett. **99**, 246403 (2007).

[36] W. Chen and A. Pasquarello, Accurate band gaps of extended systems via efficient vertex corrections in *GW*, Phys. Rev. B **92**, 041115(R) (2015).

[37] A. Tal, W. Chen, and A. Pasquarello, Vertex function compliant with the Ward identity for quasiparticle self-consistent calculations beyond *GW*, Phys. Rev. B **103**, L161104 (2021).

[38] F. Sottile, V. Olevano, and L. Reining, Parameter-free calculation of response functions in time-dependent density-functional theory, Phys. Rev. Lett. **91**, 056402 (2003).

[39] S. Sharma, J. K. Dewhurst, A. Sanna, and E. K. U. Gross, Bootstrap approximation for the exchange-correlation kernel of time-dependent density-functional theory, Phys. Rev. Lett. **107**, 186401 (2011).

[40] M. Shishkin and G. Kresse, Self-consistent *GW* calculations for semiconductors and insulators, Phys. Rev. B **75**, 235102 (2007).

[41] A. Grüneis, G. Kresse, Y. Hinuma, and F. Oba, Ionization potentials of solids: The importance of vertex corrections, Phys. Rev. Lett. **112**, 096401 (2014).

[42] Z. Guo, F. Ambrosio, W. Chen, P. Gono, and A. Pasquarello, Alignment of redox levels at semiconductor–water interfaces, Chem. Mater. **30**, 94 (2018).

[43] F. Ambrosio, Z. Guo, and A. Pasquarello, Absolute energy levels of liquid water, J. Phys. Chem. Lett. **9**, 3212 (2018).

[44] P. S. Schmidt, C. E. Patrick, and K. S. Thygesen, Simple vertex correction improves *GW* band energies of bulk and two-dimensional crystals, Phys. Rev. B **96**, 205206 (2017).

[45] V. Fiorentini and G. Gulleri, Theoretical evaluation of zirconia and hafnia as gate oxides for Si microelectronics, Phys. Rev. Lett. **89**, 266101 (2002).

[46] A. Zangwill and P. Soven, Resonant photoemission in barium and cerium, Phys. Rev. Lett. **45**, 204 (1980).

[47] R. Del Sole, L. Reining, and R. W. Godby, GWΓ approximation for electron self-energies in semiconductors and insulators, Phys. Rev. B **49**, 8024 (1994).

[48] R. Shaltaf, T. Rangel, M. Grüning, X. Gonze, G.-M. Rignanese, and D. R. Hamann, Electronic properties of zircon and hafnon from many-body perturbation theory, Phys. Rev. B **79**, 195101 (2009).

[49] A. Tal, P. Liu, G. Kresse, and A. Pasquarello, Accurate optical spectra through time-dependent density functional theory based on screening-dependent hybrid functionals, Phys. Rev. Res. **2**, 032019(R) (2020).

[50] J. C. Ward, An identity in quantum electrodynamics, Phys. Rev. **78**, 182 (1950).

[51] A. V. Chubukov, Ward identities for strongly coupled Eliashberg theories, Phys. Rev. B **72**, 085113 (2005).

[52] F. Bruneval, F. Sottile, V. Olevano, R. Del Sole, and L. Reining, Many-body perturbation theory using the density-functional concept: Beyond the *GW* approximation, Phys. Rev. Lett. **94**, 186402 (2005).

[53] G. Kresse and J. Hafner, *Ab initio* molecular dynamics for liquid metals, Phys. Rev. B **47**, 558 (1993).

[54] G. Kresse and J. Furthmüller, Efficient iterative schemes for *ab initio* total-energy calculations using a plane-wave basis set, Phys. Rev. B **54**, 11169 (1996).

[55] See Supplemental Material at http://link.aps.org/supplemental/10.1103/PhysRevB.108.245303 for descriptions of the computational details, of the extrapolation to infinite basis set, and of corrections to the band edges of the interface components.

[56] G. Kresse and D. Joubert, From ultrasoft pseudopotentials to the projector augmented-wave method, Phys. Rev. B **59**, 1758 (1999).

[57] A. Miglio, V. Brousseau-Couture, E. Godbout, G. Antonius, Y.-H. Chan, S. G. Louie, M. Côté, M. Giantomassi, and X. Gonze, Predominance of non-adiabatic effects in zero-point renormalization of the electronic band gap, npj Comput. Mater. **6**, 167 (2020).

[58] M. Zacharias and F. Giustino, One-shot calculation of temperature-dependent optical spectra and phonon-induced band-gap renormalization, Phys. Rev. B **94**, 075125 (2016).

[59] F. Karsai, M. Engel, E. Flage-Larsen, and G. Kresse, Electron–phonon coupling in semiconductors within the *GW* approximation, New J. Phys. **20**, 123008 (2018).

[60] J. P. Perdew, K. Burke, and Y. Wang, Generalized gradient approximation for the exchange-correlation hole of a many-electron system, Phys. Rev. B **54**, 16533 (1996).

[61] S. Q. Wang and H. Q. Ye, First-principles study on elastic properties and phase stability of III–V compounds, Phys. Status Solidi B **240**, 45 (2003).

[62] M. Ettenberg and R. J. Paff, Thermal expansion of AlAs, J. Appl. Phys. **41**, 3926 (1970).

[63] S. Lakel, F. Okbi, M. Ibrir, and K. Almi, Pressure effects on the elastic and lattice dynamics properties of AlP from first-principles calculations, AIP Conf. Proc. **1653**, 020065 (2015).

[64] A. Addamiano, X-ray data for the phosphides of aluminium, gallium and indium, Acta Cryst. **13**, 505 (1960).

[65] P. Haas, F. Tran, and P. Blaha, Calculation of the lattice constant of solids with semilocal functionals, Phys. Rev. B **79**, 085104 (2009).

[66] J. Bharathan, J. Narayan, G. Rozgonyi, and G. E. Bulman, Poisson ratio of epitaxial germanium films grown on silicon, J. Electron. Mater. **42**, 40 (2013).

[67] H. Holloway, K. C. Hass, M. A. Tamor, T. R. Anthony, and W. F. Banholzer, Isotopic dependence of the lattice constant of diamond, Phys. Rev. B **44**, 7123 (1991).

[68] J. Dolbow and M. Gosz, Effect of out-of-plane properties of a polyimide film on the stress fields in microelectronic structures, Mech. Mater. **23**, 311 (1996).

[69] M. Bilal, M. Shafiq, I. Ahmad, and I. Khan, First principle studies of structural, elastic, electronic and optical properties of Zn-chalcogenides under pressure, J. Semicond. **35**, 072001 (2014).

[70] H. Karzel, W. Potzel, M. Köfferlein, W. Schiessl, M. Steiner, U. Hiller, G. M. Kalvius, D. W. Mitchell, T. P. Das, P. Blaha, K. Schwarz, and M. P. Pasternak, Lattice dynamics and hyperfine interactions in ZnO and ZnSe at high external pressures, Phys. Rev. B **53**, 11425 (1996).

[71] K. Shinozaki, T. Honma, K. Oh-ishi, and T. Komatsu, Morphology of CaF2 nanocrystals and elastic properties in transparent oxyfluoride crystallized glasses, Opt. Mater. **33**, 1350 (2011).

[72] R. M. Hazen and L. W. Finger, Calcium fluoride as an internal pressure standard in high-pressure crystallography, J. Appl. Crystallogr. **14**, 234 (1981).

[73] C. G. Van de Walle, Band lineups and deformation potentials in the model-solid theory, Phys. Rev. B **39**, 1871 (1989).

[74] S.-H. Wei and A. Zunger, Predicted band-gap pressure coefficients of all diamond and zinc-blende semiconductors: Chemical trends, Phys. Rev. B **60**, 5404 (1999).

[75] M. Engel, H. Miranda, L. Chaput, A. Togo, C. Verdi, M. Marsman, and G. Kresse, Zero-point renormalization of the band gap of semiconductors and insulators using the projector augmented wave method, Phys. Rev. B **106**, 094316 (2022).

[76] H. Wang, A. Tal, T. Bischoff, P. Gono, and A. Pasquarello, Accurate and efficient band-gap predictions for metal halide perovskites at finite temperature, npj Comput. Mater. **8**, 1 (2022).

[77] I. Vurgaftman, J. R. Meyer, and L. R. Ram-Mohan, Band parameters for III–V compound semiconductors and their alloys, J. Appl. Phys. **89**, 5815 (2001).

[78] Y. P. Varshni, Temperature dependence of the energy gap in semiconductors, Physica **34**, 149 (1967).

[79] W. Bludau, A. Onton, and W. Heinke, Temperature dependence of the band gap of silicon, J. Appl. Phys. **45**, 1846 (1974).

[80] A. Mang, K. Reimann, St. Rübenacke, and M. Steube, Two-photon spectroscopy study of ZnS and CdS under hydrostatic pressure, Phys. Rev. B **53**, 16283 (1996).

[81] E. L. Shirley, Many-body effects on bandwidths in ionic, noble gas, and molecular solids, Phys. Rev. B **58**, 9579 (1998).

[82] G. W. Rubloff, Far-ultraviolet reflectance spectra and the electronic structure of ionic crystals, Phys. Rev. B **5**, 662 (1972).

[83] S. Lebègue, B. Arnaud, M. Alouani, and P. E. Bloechl, Implementation of an all-electron *GW* approximation based on the projector augmented wave method without plasmon pole approximation: Application to Si, SiC, AlAs, InAs, NaH, and KH, Phys. Rev. B **67**, 155208 (2003).

[84] J. Klimeš, M. Kaltak, and G. Kresse, Predictive *GW* calculations using plane waves and pseudopotentials, Phys. Rev. B **90**, 075125 (2014).

[85] A. Tal, W. Chen, and A. Pasquarello, Vertex function compliant with the Ward identity for quasiparticle self-consistent calculations beyond *GW*, Materials Cloud Archive **2021.140** (2021).

[86] W. Chen and A. Pasquarello, Band-edge levels in semiconductors and insulators: Hybrid density functional theory versus many-body perturbation theory, Phys. Rev. B **86**, 035134 (2012).

[87] W. Kaiser, W. G. Spitzer, R. H. Kaiser, and L. E. Howarth, Infrared properties of CaF_2, SrF_2, and BaF_2, Phys. Rev. **127**, 1950 (1962).

[88] Y. Ma and M. Rohlfing, Quasiparticle band structure and optical spectrum of CaF_2, Phys. Rev. B **75**, 205114 (2007).

[89] M. A. Olmstead, R. I. G. Uhrberg, R. D. Bringans, and R. Z. Bachrach, Photoemission study of bonding at the CaF_2-on-Si(111) interface, Phys. Rev. B **35**, 7526 (1987).

[90] M. Bertocchi, E. Luppi, E. Degoli, V. Véniard, and S. Ossicini, Large crystal local-field effects in second-harmonic generation of a Si/CaF_2 interface: An *ab initio* study, Phys. Rev. B **86**, 035309 (2012).

[91] T. Bischoff, I. Reshetnyak, and A. Pasquarello, Band alignment at the $CaF_2/Si(111)$ interface through advanced electronic structure calculations, Materials Cloud Archive **2020.74** (2020).

[92] F. Giustino and A. Pasquarello, Theory of atomic-scale dielectric permittivity at insulator interfaces, Phys. Rev. B **71**, 144104 (2005).

[93] N. A. Richter, S. Sicolo, S. V. Levchenko, J. Sauer, and M. Scheffler, Concentration of vacancies at metal-oxide surfaces: Case study of MgO(100), Phys. Rev. Lett. **111**, 045502 (2013).

[94] S. Nagao, T. Fujimori, H. Gotoh, H. Fukushima, T. Takano, H. Ito, S. Koshihara, and F. Minami, Type-II photoluminescence from GaP/AlP/GaP quantum wells, J. Appl. Phys. **81**, 1417 (1997).

[95] M. K. Kelly, D. W. Niles, E. Colavita, G. Margaritondo, and M. Henzler, Valence-band discontinuities at AlAs-based heterojunction interfaces, Appl. Phys. Lett. **46**, 768 (1985).

[96] J. R. Waldrop, E. A. Kraut, S. P. Kowalczyk, and R. W. Grant, Valence-band discontinuities for abrupt (110), (100), and (111) oriented Ge-GaAs heterojunctions, Surf. Sci. **132**, 513 (1983).

[97] S. P. Kowalczyk, E. A. Kraut, J. R. Waldrop, and R. W. Grant, Measurement of ZnSe–GaAs(110) and ZnSe–Ge(110) heterojunction band discontinuities by x-ray photoelectron spectroscopy (XPS), J. Vac. Sci. Technol. **21**, 482 (1982).

[98] P. Perfetti, F. Patella, F. Sette, C. Quaresima, C. Capasso, A. Savoia, and G. Margaritondo, Experimental study of the GaP-Si interface, Phys. Rev. B **30**, 4533 (1984).

[99] F. J. Himpsel, U. O. Karlsson, J. F. Morar, D. Rieger, and J. A. Yarmoff, Determination of interface states for CaF_2/Si(111) from near-edge x-ray-absorption measurements, Phys. Rev. Lett. **56**, 1497 (1986).

[100] D. Rieger, F. J. Himpsel, U. O. Karlsson, F. R. McFeely, J. F. Morar, and J. A. Yarmoff, Electronic structure of the CaF_2/Si(111) interface, Phys. Rev. B **34**, 7295 (1986).

[101] A. Izumi, Y. Hirai, K. Tsutsui, and N. S. Sokolov, Study of band offsets in CdF2/CaF2/Si(111) heterostructures using x-ray photoelectron spectroscopy, Appl. Phys. Lett. **67**, 2792 (1995).

[102] M. E. Lazzouni, M. Peressi, and A. Baldereschi, Valence-band offset at the Si/GaP (110) interface, Appl. Phys. Lett. **68**, 75 (1996).

[103] M. A. Olmstead, R. I. G. Uhrberg, R. D. Bringans, and R. Z. Bachrach, Initial formation of the interface between a polar insulator and a nonpolar semiconductor: CaF_2 on Si(111), J. Vac. Sci. Technol. B **4**, 1123 (1986).

[104] F. Xu, M. Vos, and J. H. Weaver, Influence of au overlayers on valence-band offsets for buried CaF_2/Si(111) interfaces, Phys. Rev. B **39**, 8008 (1989).